Cluster observations of multiple dipolarization fronts

K.-J. Hwang,[1,2] M. L. Goldstein,[1] E. Lee,[3] and J. S. Pickett[4]

Received 31 May 2010; revised 31 January 2011; accepted 4 February 2011; published 13 April 2011.

[1] We present Cluster observations of a series of dipolarization fronts (DF 1 to 6) at the central current sheet in Earth's magnetotail. The velocities of fast earthward flow following behind each DF 1–3 are comparable to the Alfvén velocity, indicating that the flow bursts might have been generated by bursty reconnection that occurred tailward of the spacecraft. Based on multispacecraft timing analysis, DF normals are found to propagate mainly earthward at 160–335 km/s with a thickness of 900–1500 km, which corresponds to the ion inertial length or gyroradius scale. Each DF is followed by significant fluctuations in the x and y components of the magnetic field whose peaks are found 1–2 min after the DF passage. These (B_x, B_y) fluctuations propagate dawnward (mainly) and earthward. Strongly enhanced field-aligned beams are observed coincidently with (B_x, B_y) fluctuations, while an enhancement of cross-tail currents is associated with the DFs. From the observed pressure imbalance and flux tube entropy changes between the two regions separated by the DF, we speculate that interchange instability destabilizes the DFs and causes the deformation of the midtail magnetic topology. This process generates significant field-aligned currents and might power the auroral brightening in the ionosphere. However, this event is associated with neither the main substorm auroral breakup nor the poleward expansion, which might indicate that the observed multiple DFs have been dissipated before they reach the inner plasma sheet boundary.

Citation: Hwang, K.-J., M. L. Goldstein, E. Lee, and J. S. Pickett (2011), Cluster observations of multiple dipolarization fronts, *J. Geophys. Res.*, *116*, A00I32, doi:10.1029/2010JA015742.

1. Introduction

[2] Dipolarization fronts (DFs) are a phenomenon commonly detected near the equatorial plane of the Earth's tail plasma sheet. The term refers to a plasma boundary that separates an earthward flux tube having a significant B_z component from the ambient inner plasma sheet. DFs are characterized by a sharp jump in B_z, a density drop, and often a following earthward fast flow (called bursty bulk flows, or BBFs) [*Ohtani et al.*, 1992; *Angelopoulos et al.*, 1999; *Lui et al.*, 1992; *Nakamura et al.*, 2002b; *Slavin et al.*, 2003; *Shiokawa et al.*, 2005; *Runov et al.*, 2009; *Sergeev et al.*, 2009]. One possible mechanism of the generation of DFs is near-Earth reconnection that causes abruptly increased magnetic fluxes to be transported earthward, and creates a magnetic pileup region earthward of the reconnection site [*Hoshino et al.*, 2001; *Hoshino*, 2005; *Nakamura et al.*, 2009; *Sitnov et al.*, 2009].

[3] DFs detected by a local in situ observation do not necessarily refer to substorm dipolarization, a global feature referring to that the Earth's tail magnetic configuration becomes more dipolar, but, are often associated with the global substorm phenomenon. In the substorm dynamics, dipolarization of tail magnetic topology is preceded by the plasma sheet thinning. The nightside plasma sheet can thin from its dipole topology mainly due to the enhanced dayside-to-nightside convection of flux tubes that will compress the tail lobes and the plasma sheet. The thinning of the plasma sheet can endue various midtail instabilities, including the tearing mode (and reconnection), and current-driven and interchange or ballooning instabilities in the transition region between the dipole-like inner and the taillike outer plasma sheet. The inner edge of the transition region is where the BBFs brake into dawnward/duskward flows due to a strong pressure gradient [*Shiokawa et al.*, 1997]. Such a diversion of flows can give rise to vortical flows in the dawn and/or dusk sides from the midnight meridian [*Birn and Hesse*, 1991; *Keiling et al.*, 2009]. The inner edge of the transition region is also where cross-tail current disruption is initiated [*Lui*, 1996]. The resulting flow diversion and magnetic field disturbances produce field-aligned currents that can feed the substorm breakup arc. Therefore, this region is often thought to be a magnetospheric counterpart of the ionospheric substorm onset location.

[1]NASA Goddard Space Flight Center, Greenbelt, Maryland, USA.
[2]Goddard Earth and Sciences Technology Center, University of Maryland at Baltimore County, Baltimore, Maryland, USA.
[3]Department of Astronomy and Space Science, Kyung Hee University, Yong-In, South Korea.
[4]Department of Physics and Astronomy, University of Iowa, Iowa City, Iowa, USA.

Copyright 2011 by the American Geophysical Union.
0148-0227/11/2010JA015742

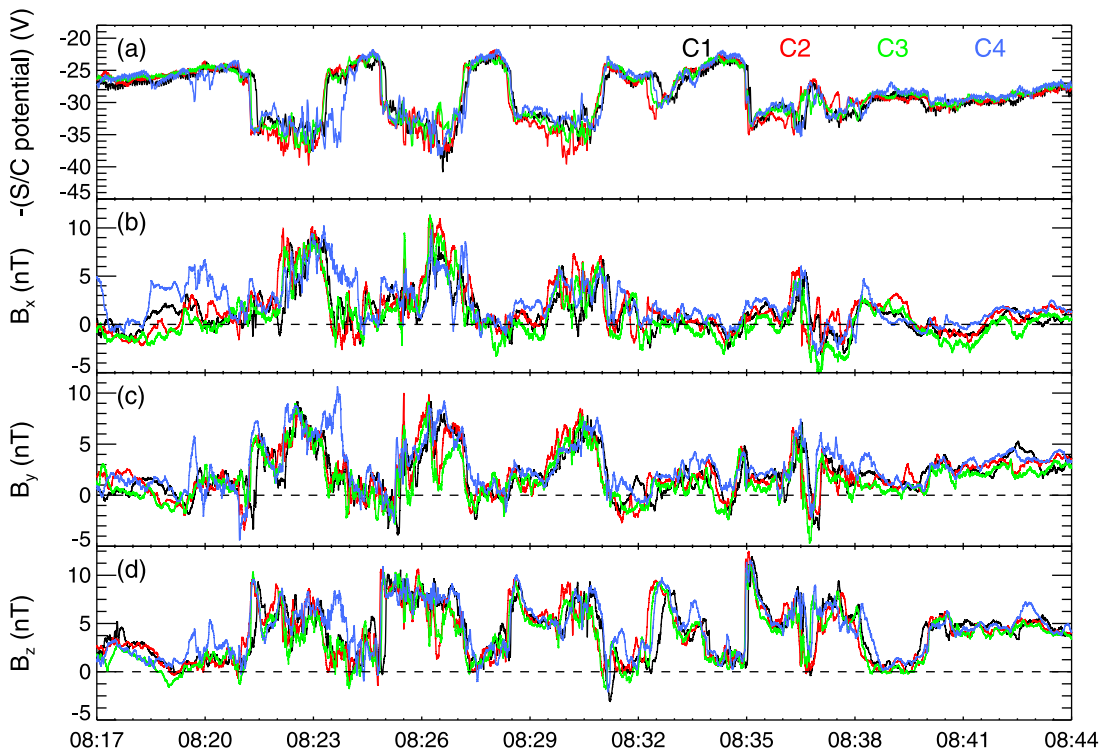

Figure 1. The four Cluster spacecraft observations during 15 August 2001, 0817–0844 UT. (a) Negative of the spacecraft potential that is indicative of the electron density [*Pedersen et al.*, 2008] and (b-d) the magnetic field components in the x_{GSM}, y_{GSM}, and z_{GSM} directions. Cluster 1 (C1) data are shown in black, and C2, C3, and C4 data are shown in red, green, and blue, respectively.

[4] Although the relationship of DFs and/or BBFs to substorms is still under debate, recently, *Runov et al.* [2009] reported a THEMIS observation of earthward propagation of a DF through the transition region from $X_{GSM} = -20\ R_E$ to $X_{GSM} = -11\ R_E$. An auroral structure was linked to the earthward DF and BBF using THEMIS All-Sky Imager data [*Runov et al.*, 2011].

[5] In this paper, we present Cluster observations of multiple DFs near the neutral sheet in the Earth's magnetotail. Detailed analyses using data from the four Cluster spacecraft suggest that the DFs are earthward injection boundaries of low-content (low-entropy) flux tubes that have been possibly generated by bursty/transient reconnection tailward of the observation location. Significant fluctuations in the x and y components of the magnetic field following a DF passage indicate a midtail magnetic field reconfiguration, which is found to be associated with enhanced field-aligned currents. Under these observations, we speculate that interchange instability perturbs the DF, leading to deformation of the midtail magnetic topology. This deformation in turn generates field-aligned currents, and can power the substorm auroral brightening.

[6] In section 2, we present an overview of the event (section 2.1) and investigate propagation properties of DFs and following (B_x, B_y) fluctuations (section 2.2). In section 2.3, we discuss cross-tail/field-aligned current enhancements that are associated with DFs and (B_x, B_y) fluctuations. Investigations on the microscopic physical processes occurring at a DF and within the injection flux tube are followed in section 2.4, where we examine particle behavior and the wave characteristics associated with these magnetic disturbances. Finally, we discuss the flux tube entropy of the injection flux tubes to explain the development of tail magnetic reconfiguration. We conclude this paper with a discussion and future study in section 3.

2. Observations

2.1. Overview of the Event

[7] On 15 August 2001, the four Cluster spacecraft were located near the tail neutral sheet. The barycenter of the quartet was at (−18.1, −5.4, 0.8) Earth radii (R_E) in geocentric solar magnetospheric (GSM) coordinates. The spacecraft observed repeated magnetic pileup patterns as shown in Figure 1. We use the negative of the spacecraft potential as a proxy for the electron density [*Pedersen et al.*, 2008]. Figure 1a shows a sharp drop in the density and Figure 1d shows a steep northward B_z buildup. These features, i.e., a sharp B_z jump with a density drop are characteristic of a DF. Note that coincident with the fluctuations in B_z, comparable fluctuations in B_x and B_y (Figures 1b and 1c) are observed. The peaks of these (B_x, B_y) fluctuations follow the DF passage by about 1–2 min.

[8] High Resolution OMNI data from ACE reveal that the event marked by red vertical lines in Figure 2 occurred within a relatively inactive and stationary period of B_y-dominant IMF conditions, but under slightly southward B_z (Figure 2a). A peak in the AE index at ~0836 UT (see Figure 2e) is associated with ionospheric auroral activity as seen by the

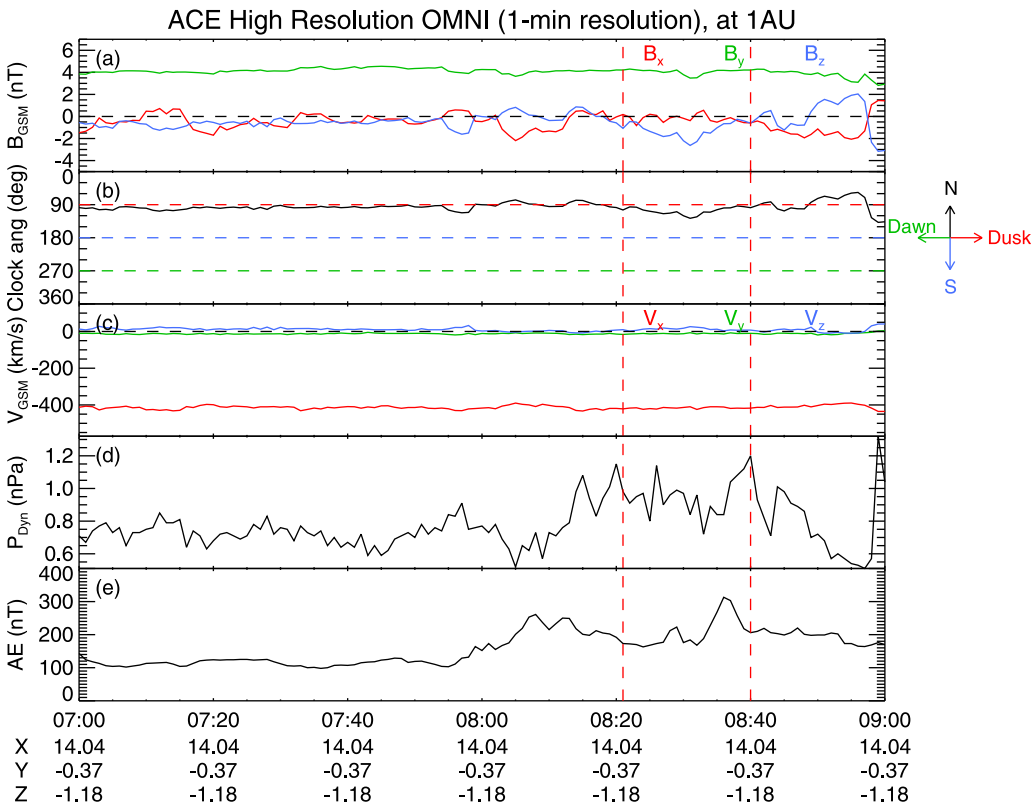

Figure 2. ACE High Resolution OMNI data at 1 min. resolution around the event marked by red vertical lines: (a) the interplanetary magnetic field (IMF) components, B_x, B_y, and B_z, in red, green, and blue, respectively; (b) IMF clock angle; (c) solar wind flow velocity; (d) solar wind dynamic pressure; and (e) AE index.

far ultraviolet (FUV) instrument on IMAGE [*Mende et al.*, 2000] (see Figure 3).

[9] Figure 4 shows the detailed field and plasma signatures of the event from Cluster 1 (C1): the magnetic field (Figure 4a), $|\mathbf{B}BB|$ (black), B_x (red), B_y (green), and B_z (blue); the ion energy spectrogram (Figure 4b); the electron energy spectrogram (Figure 4c); the electron pitch angle distribution (Figure 4d); the wave spectral power density from the electric field (the Doppler-shifted lower hybrid (f_{lh}) and electron cyclotron (f_{ce}) frequencies are denoted as black and yellow curves [cf. *Sahraoui et al.*, 2009]) (Figure 4e); the characteristic energy (Figure 4f), defined as the energy flux divided by the number flux, for ions (black) and electrons (blue) (these characteristic energies are also plotted in Figures 4b and 4c); the ion density of H^+ (black) and O^+ (red) (Figure 4g); the ion parallel (green) and perpendicular (red) temperatures (Figure 4h); the plasma β defined by the ratio of the plasma pressure to the magnetic pressure (Figure 4i); the plasma (red) and magnetic (blue) pressures, and the sum of plasma and magnetic pressures (black) (Figure 4j); the entropy calculated from the ion distribution function (Figure 4k), i.e., $S = -k_B \int F \ln F d^3\mathbf{v} d^3\mathbf{r}$ (black), and the entropy parameter or "flux tube entropy" defined by PV^{γ} (red), where γ is assumed to be 5/3 based on temperature isotropy, derived using *Wolf et al.*'s [2006] formula for the estimation of the volume of a closed flux tube, $V = \int ds/B$ (the green curve shows one third of the estimated flux tube volume in R_E/nT), and the specific flux tube entropy using theion density, i.e., $P/n^{5/3}$ (blue) (note that the entropy parameter is related to thermodynamic entropy such that $PV^{5/3} \propto \exp(2S/3)$); the electric field, E_x (red), E_y (green), and E_z (blue) (Figure 4l);the ion velocity, V_x (red), V_y (green), and V_z (blue), where the local Alfvén velocity is shown in magenta (Figure 4m). All the parameters are shown in GSM coordinates throughout this paper. The DFs (1–6) and (B_x, B_y) fluctuation structures (a to d) are marked at the top of Figure 4a. (Although fluctuations in B_z exist following the DFs, we refer to these structures as "(B_x, B_y) fluctuations" for convenience.)

[10] The overview plot shows typical signatures of the DFs, such as a sharp B_z jump (Figure 4a) with a density drop (Figures 1a and 4g), a corresponding decreases in β (Figure 4i), a plasma pressure decrease, and a magnetic pressure increase (Figure 4j) across each DF as indicated by a magenta vertical line. For DFs 1–3 (and, possibly DF 5) earthward fast flows follow 1.5–2 min after each DF passage (Figure 4m). The largest velocities of these earthward flows are comparable to the Alfvén velocity.

[11] In this event there are significant B_x and B_y fluctuations that peak about 1–2 min after passage of the DFs (Figure 4a). Also note that the ion characteristic energy increases while the electron characteristic energy decreases across a DF (most clearly seen for DF 1, 3, and 5 in Figure 4f), unlike other DF in situ observations that have been detected primarily in the inner magnetospheric plasma sheet where both electrons and ions become energized

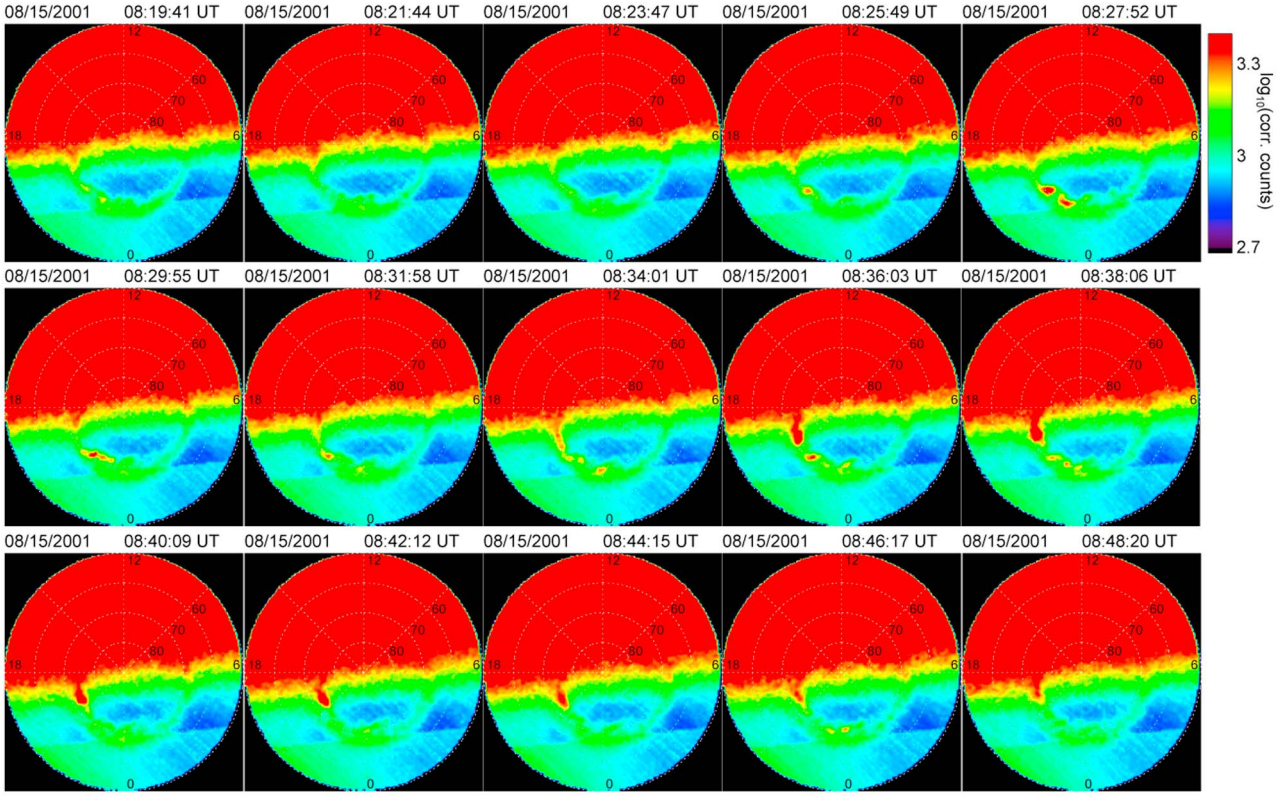

Figure 3. The far ultraviolet (FUV) image of the global view of the polar region in the Earth's Northern Hemisphere from Wideband Image Camera (WIC) onboard the IMAGE satellite. The coordinate system is the geomagnetic coordinates (MAG).

behind a DF [*Runov et al.*, 2009; *Zhou et al.*, 2009; *Sergeev et al.*, 2009]. The electrostatic broadband noise is enhanced between the lower hybrid frequency and a few times the electron cyclotron frequency (Figure 4d) and electron solitary-wave structures (not shown) are also found during the event. In sections 2.3, 2.4 and 3, we will discuss the microphysical properties associated with the DFs as evidenced by the sharp peaks in E_x (Figure 4l) together with particle distribution functions and wave characteristics, and the observed (flux tube) entropy decreases (Figure 4k) across the DFs.

2.2. Propagation and Normal of DFs and B_{xy} Fluctuations

[12] In this section we examine the propagation velocities along the boundary normals and normal directions of the six DFs (1–6) and four (B_x, B_y) structures (a-d). Figure 5 shows the relative location of the four spacecraft around their barycenter in the XY_{GSM} plane at the times of DF 1, 2, 3 and 5 (Figure 5, top) and (B_x, B_y) fluctuation structures a, b, c, and d (Figure 5, bottom) observations. The thick gray arrows represent the XY_{GSM} plane projections of the propagation velocities along the boundary normal determined by multispacecraft magnetic field minimum variance analysis (MVA) [*Paschmann and Daly*, 1998], the magenta arrows of the normal directions determined by magnetic field minimum variance analysis [*Paschmann and Daly*, 1998], and the green arrows of bulk flow velocities at the maximum of the BBFs from C1 and C3. The lengths of the velocity vectors shown at the top right corner in the first panel correspond to a flow speed of 500 km/s (green) and a propagation speed of 100 km/s (grey). (Note that both four-spacecraft timing analysis and minimum variance analysis on the boundaries assume that the boundary front is nearly planar and quasi-stationary. The timing analysis that gives the propagation velocity projected along the boundary normal further assumes that the front moves with constant velocity over the scale of the spacecraft separation.)

[13] Table 1 summarizes the propagation and normal signatures of the DFs and (B_x, B_y) fluctuations. We use the timings of the four spacecraft passages of a sharp B_z jump for the propagation of the DFs. For (B_x, B_y) fluctuations, the time series over each period among the four spacecraft are not identical enough to read the timings by a visual inspection. The timings are, therefore, determined based on the time shifts that give best correlations between the time series measured from the four spacecraft. The normal propagation velocity (V_{prop}) and the time difference (Δt, typically a few seconds, not shown) of B_z minimum to maximum at the DF are used to derive the thickness of the DFs, Δl ($\Delta l = V_{prop} \times \Delta t$). The angle, θ, between the normal propagation direction ($\hat{V}_{prop}$) and the boundary normal averaged over the spacecraft ($\hat{N}_{av}$) is relatively small ($\lesssim 19°$) for DFs 1–5, and (B_x, B_y) fluctuations b-d, which justifies the assumptions of planarity and stationarity. Indeed, normals from the multiple spacecraft well concur for these structures, supporting the assumption of planarity. DF 6 and

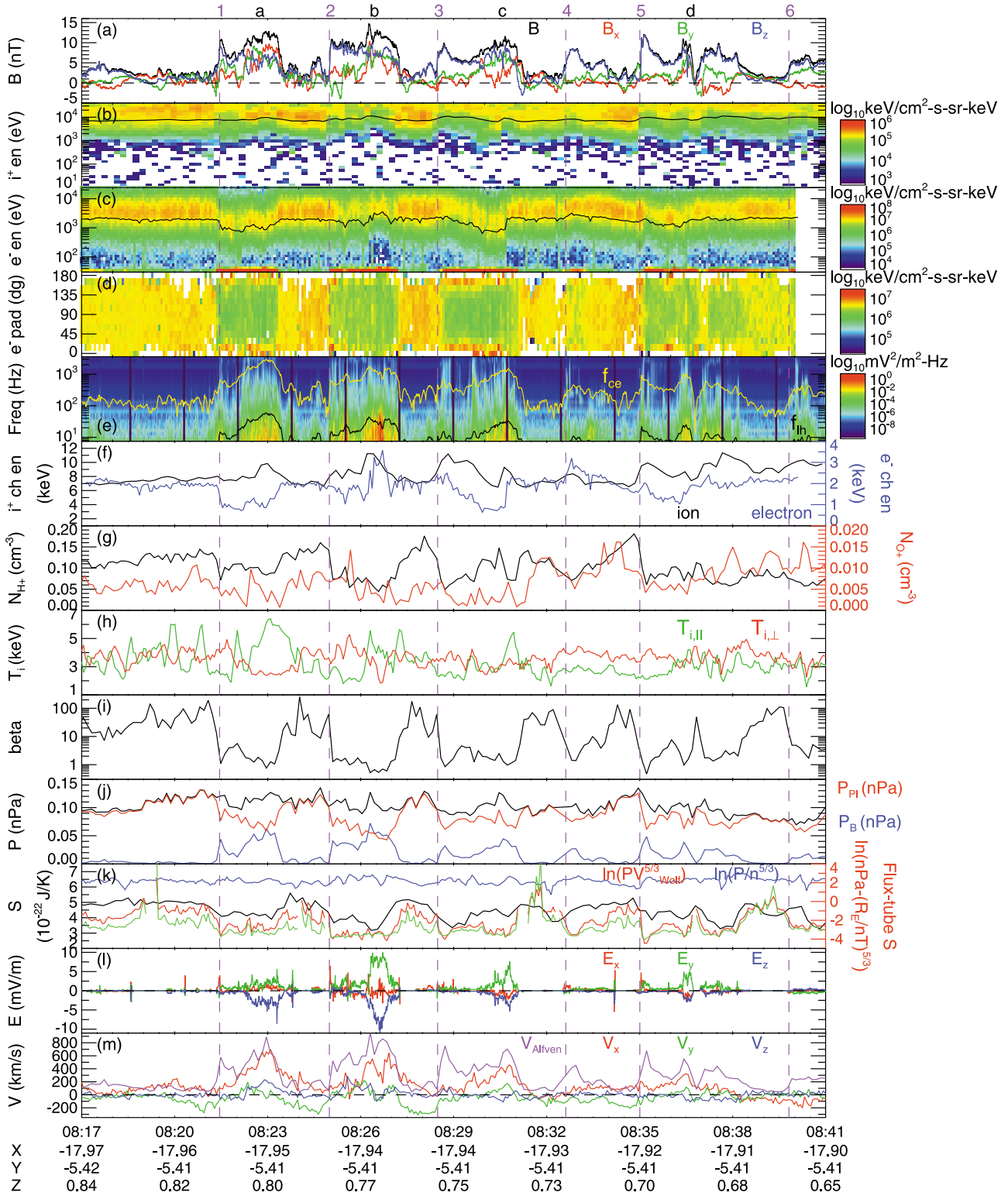

Figure 4. (a-m) Overview of the event from C1 observation. Details are found in the text.

(B_x, B_y) fluctuations "a" show larger θ values (up to ~44°), meaning either that the structures are not close to planar on the scale of the spacecraft separation, or that they undergo temporal variations as the DF passes between the spacecraft. Nevertheless, the normal of DF 6 or (B_x, B_y) fluctuations "a" from the four spacecraft are similar (the standard deviation in the normal vector obtained at the four-spacecraft locations is <0.23), indicating that temporal effects are a more

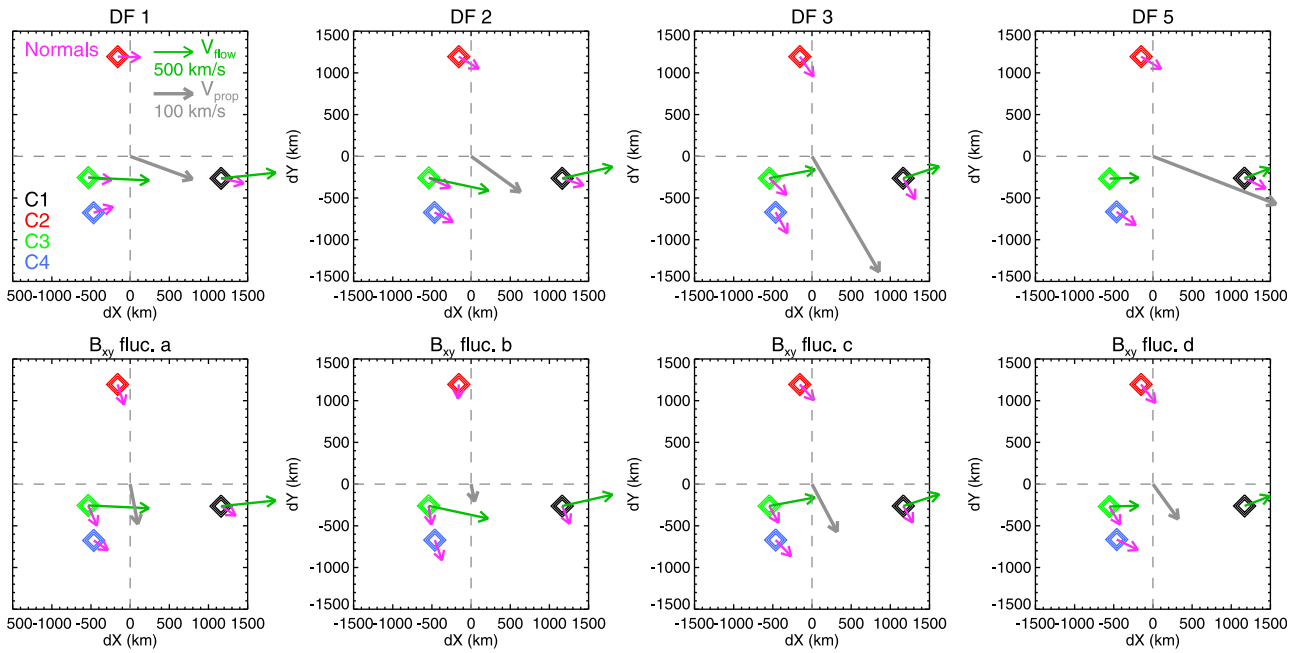

Figure 5. The relative location of the four spacecraft around its barycenter in (top) the XY_{GSM} plane at the times of DF 1, 2, 3, and 5 and (bottom) the (B_x, B_y) fluctuation structures a, b, c, and d observations. Details are described in the text. The normals of C3 at DF 5 and C1 at (B_x, B_y) fluctuation d are discarded since the medium-to-minimum eigenvalue ratio in the minimum variance calculation is below 1.5. For all other normals noted above, the medium-to-minimum ratio is greater than 3.

probable cause for the large θ values. Both MVA normals and normal propagation directions of the (B_x, B_y) fluctuations make a noticeable oblique angle off the near-equatorial plane toward the magnetic north pole with comparison to the DFs.

[14] Figure 5 and Table 1 demonstrate that the DFs propagate mostly earthward and slightly dawnward, and indicate that the (B_x, B_y) fluctuation normals are mostly dawnward and a bit earthward at lower speeds than DFs. For DF 3, a further diversion to the dawnward direction is observed, which might be due to the pressure of the inner magnetosphere plasmas near the midnight meridian that have been compressed and/or heated by the preceding two DFs. Recall that because multiple DFs can arise from bursty/patchy reconnection, changes in the topology of the reconnection X line from which each DF might have originated can give rise to different DF motions. DF 6, which shows a gradual and smaller B_z increase, retreats tailward. Tailward propagation of dipolarization is expected when the pileup of the reconnected magnetic flux continues while the inner edge of the pileup region is stationary [*Birn and Hesse*, 1991], or when the reconnection X line moves tailward faster than the earthward motion of the reconnected flux tubes. Such tailward DF propagation can be related to the global relaxation of a thinned plasma sheet that is recovering a more dipolar shape as is expected during substorm recovery. Small-scale auroral structures detected by the IMAGE FUV camera indeed disappear in a few minutes of the Cluster observation of DF 6 (see Figure 3). However, the bright blobs shown in Figure 3 show neither a main substorm breakup nor any clear poleward expansion. These *pseudobreakup*-like signatures are discussed further in

Table 1. A Summary of the Propagation and Normal Properties of the DFs and (B_x, B_y) Fluctuations[a]

DF/B_{xy} Fluctuation	V_{prop} (km/s)	$\hat{V}_{prop}$ (GSM)	$\hat{N}_{av}$ (GSM)	$\theta(\hat{V}_{prop}, \hat{N}_{av})$	Thickness (km)
DF 1	170.1	(0.94, −0.32, −0.15)	(0.95, −0.04, −0.27)	18.9	1457
DF 2	160.1	(0.79, −0.53, −0.31)	(0.86, −0.38, −0.30)	13.5	922
DF 3	327.2	(0.52, −0.85, 0.09)	(0.58, −0.79, 0.16)	9.6	1526
DF 4	71.3	(0.77, −0.63, 0.11)	(0.60, −0.77, 0.10)	16.8	1542
DF 5	334.9	(0.94, −0.34, −0.01)	(0.86, −0.48, −0.17)	13.7	1048
DF 6	118.0	(−0.99, −0.02, −0.10)	(−0.70, 0.54, −0.34)	44.1	
B_{xy} a	108.6	(0.18, −0.88, 0.43)	(0.47, −0.60, 0.25)	43.9	
B_{xy} b	105.4	(0.17, −0.79, 0.59)	(0.25, −0.76, 0.59)	7.7	
B_{xy} c	135.7	(0.47, −0.84, 0.26)	(0.52, −0.65, 0.53)	21.8	
B_{xy} d	111.6	(0.58, −0.75, 0.31)	(0.66, −0.63, 0.24)	21.6	

[a]The normal propagation velocity (V_{prop}), the angle (θ) between the normal propagation direction ($\hat{V}_{prop}$) obtained from four-spacecraft timing analysis and the normal direction using magnetic field minimum variance analysis averaged over the spacecraft ($\hat{N}_{av}$), and the time difference (Δt, not shown) of B_z minimum to maximum at the DF are used for the derivation of the thickness of the DFs, Δl ($\Delta l = V_{prop} \times \Delta t$).

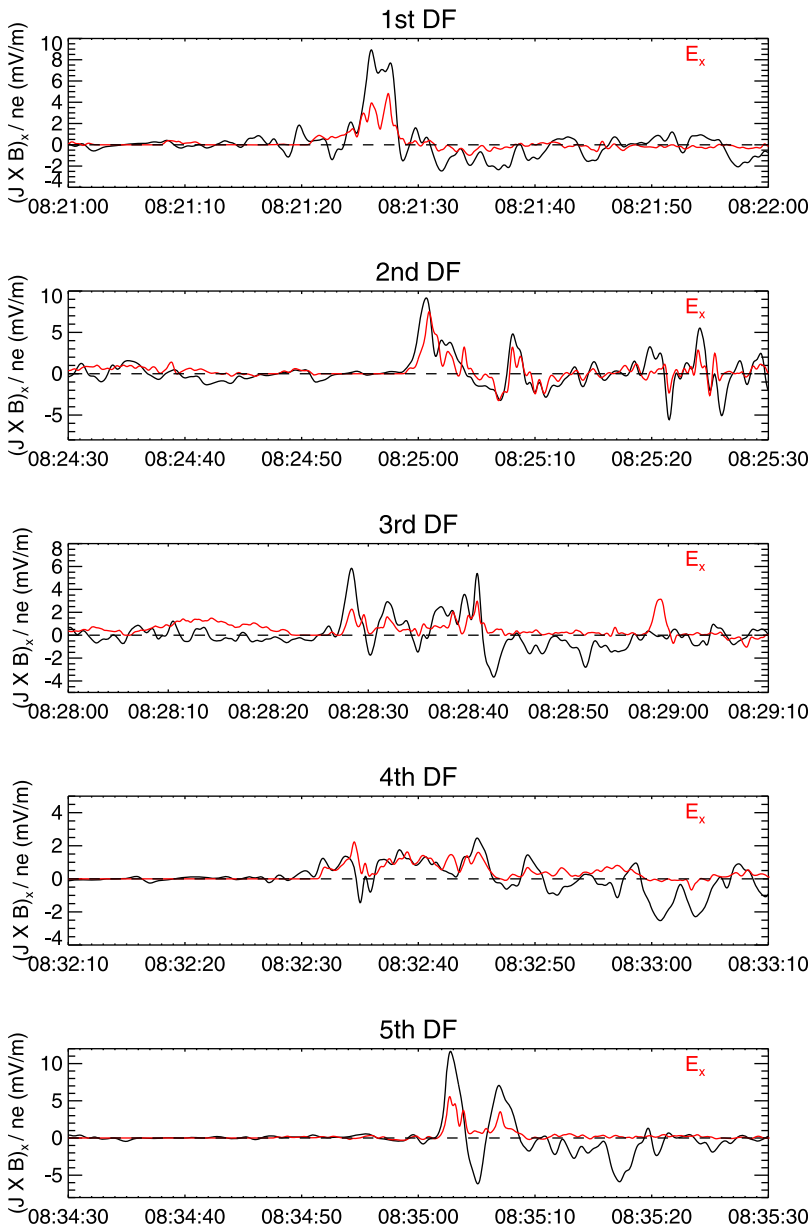

Figure 6. Comparison of the x component of Hall electric field, BJ × BB/ne, where n (e) is the electron density (charge) shown in black, and E_x in the plasma inertial frame (in red) observed at the exact location of DF 1–5.

section 3. On the other hand, *Guzdar et al.* [2010] have suggested that a mushroom-like structure can arise from the development of a Rayleigh-Taylor or interchange instability that would account for the observed tailward retreat of a DF that follows the earthward propagation of a preceding DF.

[15] We find that the typical thickness of the DFs is comparable to the ion inertial length, $\lambda_i \approx$ 900–1400 km, or the ion gyroradius (0.8–1.7 × λ_i), which indicates that Hall effects may be important at the DF. From Figure 6 the sharp peaks of E_x in the plasma inertial frame are observed at the exact location of DF 1–5 (Figure 4l) with amplitudes that are approximately what is expected for the Hall electric field. (The derivative of the magnetic field along the C1 trajectory was used to estimate the current in calculating the Hall electric field to compare it to the electric field measured from C1.) Demagnetization of ions (with magnetized electrons at such ion scales) can lead to ion-electron decoupling at the DF, which can generate drift-type instabilities and waves that may be the process that generates the enhanced wave emissions observed at the DFs shown in Figure 4e.

[16] In section 2.3 we discuss how these magnetic disturbances are related to the generation and enhancement of midtail local currents.

2.3. Current Enhancement Associated With the DFs and (B_x, B_y) Fluctuations

[17] We used the curlometer technique [*Paschmann and Daly*, 1998] to derive the currents associated with the DFs and (B_x, B_y) fluctuations. The ratio $\nabla \cdot \mathbf{B}BB/|\nabla \times \mathbf{B}BB|$ (Figure 7f) indicates the quality check of the curlometer

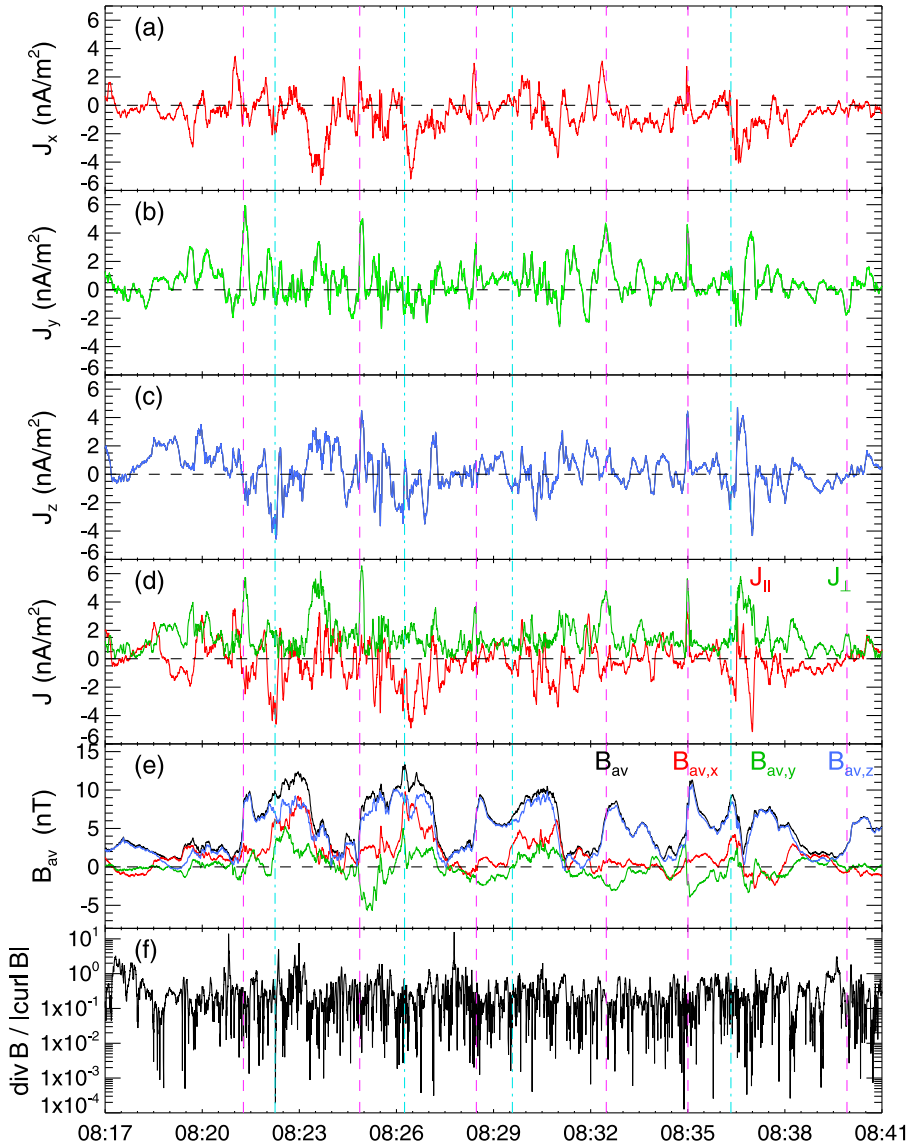

Figure 7. Current densities, derived using a curlometer technique [*Paschmann and Daly*, 1998], associated with the magnetic disturbances during the event: (a-c) the x_{GSM}, y_{GSM}, and z_{GSM} components of the calculated current density; (d) the current density, parallel (red) and perpendicular (green) to the magnetic field; (e) the averaged magnetic field over the four spacecraft; and (f) divergence of the magnetic field divided by the curl of it, indicative of the reliability of the curlometer technique (the results become less reliable when this value becomes further greater than 0).

technique (the results become less reliable as this value becomes further greater than 0) [*Paschmann and Daly*, 1998]. Figure 7 shows that the DF is associated with the cross-tail current enhancement, while the (B_x, B_y) fluctuations are associated with enhancement of the field-aligned current.

[18] The peaks up to 6.6 nA/m^2 in the current perpendicular to the magnetic field ($J_\perp$ in Figure 7d at the times of the 6 DFs indicated by magenta vertical dashed lines) correspond to positive peaks in J_y (Figure 7b). DF 6, however, shows a much smaller increase in the dawnward cross-tail current (negative J_y). This cross-tail current-density enhancement can be explained by a diamagnetic effect ($\mathbf{B}BJ = \mathbf{B}BB \times \nabla P/B^2$) due to the compression of plasmas ahead of the DF ($\nabla P > 0$, along $\hat{V}_{prop}$) [*Runov et al.*, 2009].

[19] Figure 8 shows particle distribution functions immediately ahead of (or almost at) (Figures 8a–8c) and behind (Figures 8d–8f) DF 1 for electrons and ions. Two-dimensional electron pitch angle distributions (Figures 8a, 8d, and 8g) and Fig22-D cuts of 3-D ion distribution functions are presented. A decrease in temperature across the DF is observed in electrons along with $T_\perp > T_\parallel$ immediately upstream of the DF, and $T_\parallel > T_\perp$ in the downstream region. This temperature decrease across the DF is not as clear in ions. The $T_\perp > T_\parallel$ anisotropy is more dominant in the downstream region (Figure 8e and 4h). Because the thickness of a DF is comparable to the ion gyroradius scale, perpendicularly heated ions on one side of a DF can produce

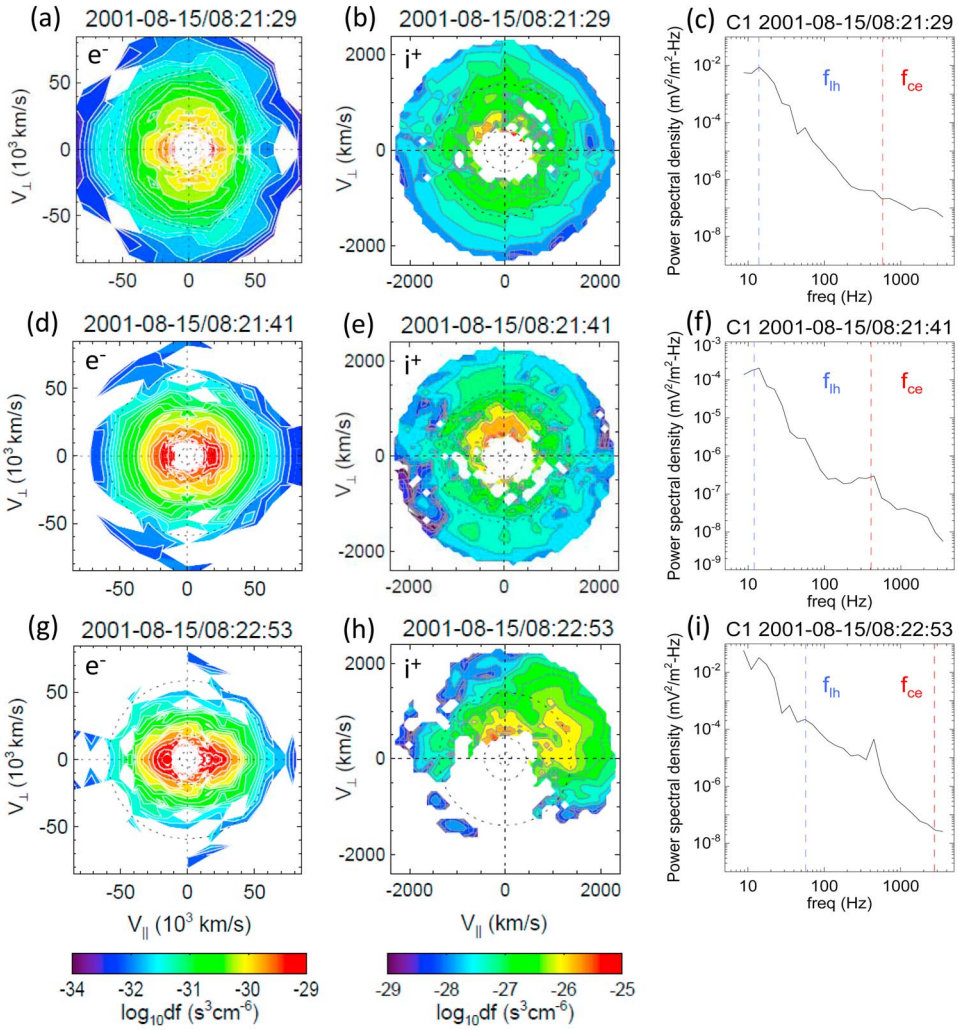

Figure 8. (a, d, and g) The electron and (b, e, and h) the ion distribution functions in the parallel (horizontal axis) and perpendicular (vertical axis) velocity space and (c, f, and g) the electric field spectral power density where the Doppler-shifted lower hybrid (f_{lh}) and electron cyclotron (f_{ce}) frequencies are denoted. Figures 8a–8c (Figures 8d–8f) show the particle distributions and wave characteristics immediately ahead of (behind) the DF. Figures 8g–8i correspond to particle and wave features when the significant (B_x, B_y) fluctuations are observed.

a $T_\perp > T_\parallel$ on the other side of the DF. Nevertheless, the enhanced high-energy ion fluxes in the direction of a "positive" $\mathbf{B}BV_\perp$ (along the $\mathbf{B}BE \times \mathbf{B}BB$ direction, i.e., the dawnward direction at the time of Figure 8b) indicate that the ion energization mainly occurred behind the DF (see the cartoon in Figure 9a), possibly via wave-particle interactions associated with broadband low-frequency waves intensified behind the DF (to be discussed more in section 2.4).

[20] Electron distributions (at energies below ~26 keV) show perpendicular heating immediately before or almost at a DF, which is consistent with the observation of enhanced cross-tail current density produced by a net gyromotion of energized electrons close to the DF (see Figure 9a) and a diamagnetic effect associated with the density drop across the DF. Because the portion of the ions that contribute to $-J_y$ on the downstream side is smaller than that of the hotter bulk electrons that contribute to $+J_y$ on the immediately upstream region, the net current points in the direction of a normal cross-tail current ($+J_y$). Thus the charge carrier of the enhanced cross-tail current is electrons.

[21] Field-aligned currents intensify during the (B_x, B_y) fluctuations ($J_\parallel$ in Figure 7d, around the times of cyan vertical dashed lines). The currents are primarily opposite to the field direction (negative values of $J_\parallel$), mostly along the $-Z_{GSM}$ direction, and $-X_{GSM}$ direction, implying an upward field-aligned current in the ionosphere. These field-aligned currents can be associated with deformation of a magnetic topology. For example, Figure 9b illustrates that a distortion of the midtail magnetic field can be caused by a finite Y_{GSM} directional extent of a tail reconnection X line and a resulting fast flow channel. The finite extent of the earthward BBF in y causes the central (BBF meridian) field lines to become more dipolar, but the field lines away from the BBF meridian to remain stretched. Such geometry results in a magnetic shear ($\partial B_z/\partial y$ and $\partial B_x/\partial y$) that is mainly along y,

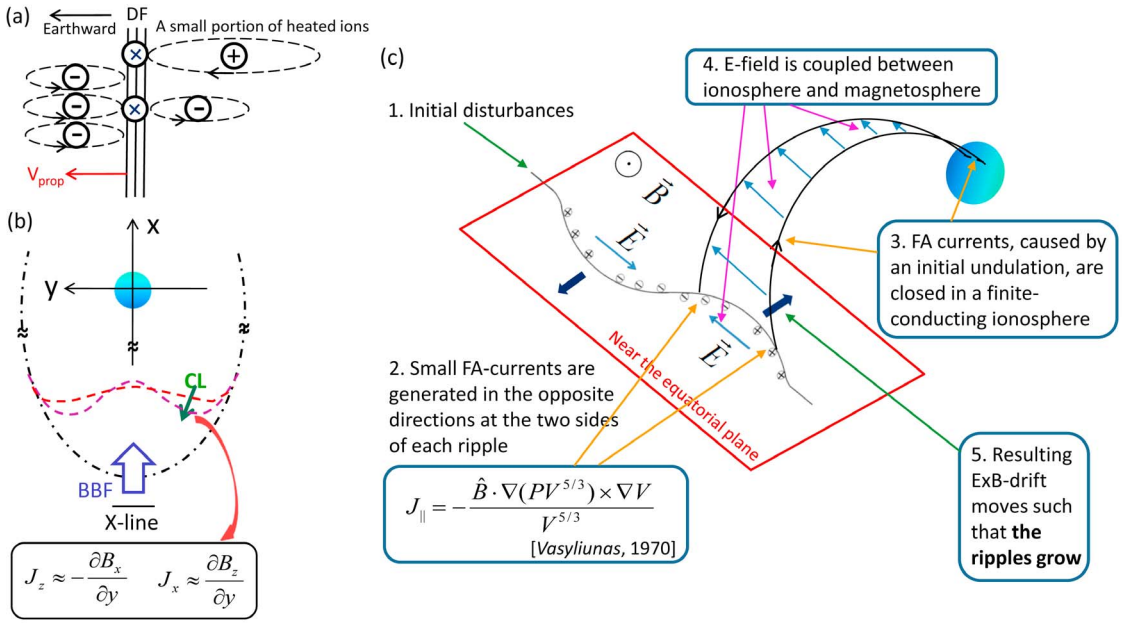

Figure 9. Illustrations of (a) particle acceleration and heating around the DF; (b) a possible midtail magnetic topology, caused by a limited Y_{GSM} directional extent of a tail reconnection X line and a resulting BBF channel, that gives rise to the field-aligned current enhancement; and (c) how MI coupling is involved in the development of interchange instability and the generation and enhancement of field-aligned currents (modified from *Xing* [2008]).

which corresponds to a current in the x and z directions, respectively.

[22] Cluster, located slightly dawnward of the midnight meridian (marked by "CL" in Figure 9b) is expected to move along the green arrow in the reference frame of the magnetic fluctuation structures, based on how the DF and (B_x, B_y) fluctuations are propagating. The red dashed line represents a more planar DF. The boundary associated with (B_x, B_y) fluctuations following the DF is denoted by a magenta dashed line. Cluster's trajectory through these structures gives rise to $\partial B_z/\partial y < 0$ and $\partial B_x/\partial y > 0$, i.e., negative J_x and J_z, consistent with the currents shown in Figure 7. J_z (Figure 7c) rather fluctuates around zero associated with the complicated B_{xy} variations. In contrast, J_x is mostly negative during these (B_x, B_y) fluctuations (Figure 7a). However, when (B_x, B_y) increases most rapidly, i.e., when the magnetic geometry starts to deform most rapidly (see the cyan vertical lines), both J_z and $J_{\parallel}$ consistently show negative values and often negative peaks. In section 3, we discuss the deformation of the injection boundary in the context of the interchange instability as the boundary evolves from that indicated by the red dashed line to the magenta dashed one.

2.4. Particle Distributions and Wave Characteristics Near the DFs and (B_x, B_y) Fluctuations

[23] Plasma behind the DF (or within the BBF flux tube) is expected to be accelerated and heated with time during an earthward convection of the DF or BBF (until it reaches a flow-braking region where a stronger magnetic field and higher plasma pressure impede its propagation) [*Sitnov et al.*, 2009]. The acceleration might occur via statistical Fermi acceleration, betatron acceleration, and/or wave-particle interactions. If a DF channel is detected close to the reconnection X line (i.e., before its earthward convection leads the flux tube behind the DF to be fully heated), the DF will appear to separate two regions: a hot and dense plasma upstream and a cold and low-density plasma downstream. (The enhanced B_z flux tube behind a DF can contain high-energy electrons outflowing from the reconnection site. However, these outflowing electrons are colder than inner plasma sheet populations.) Particle distributions across the DF (Figure 8) show that electrons ≤26 keV might undergo a perpendicular heating immediately prior to or close to the DF, while ≤40 keV ion perpendicular heating occurs further behind the DF. This implies that the mechanism of particle energization associated with a DF is different for electrons and ions, which might explain the opposite trend in the variation of the characteristic energy between electrons and ions, noticed in Figure 4f (except for DF 4). Here, we investigate small-scale physical processes that might be associated with the particle distributions and wave emission at the DF and as the (B_x, B_y) fluctuations are encountered.

[24] The electron distributions behind the DF (Figures 8d and 8g) are characterized by parallel and antiparallel field-aligned beam components, resulting in $T_{\parallel} > T_{\perp}$. This signature becomes more intense as the (B_x, B_y) fluctuations, which contain colder electrons, pass by. Electron two-stream instabilities can be generated by the observed bidirectional electron beams and such beam can generate electron solitary-wave structures [*Goldman et al.*, 1999] as were detected in WBD data (not shown) [*Pickett et al.*, 2005] downstream of the DF during the period of the (B_x, B_y) fluctuations.

[25] As seen in Figure 4e, enhanced wave emissions are present within the enhanced B_z flux tubes behind a DF over a broad frequency range from below the lower hybrid fre-

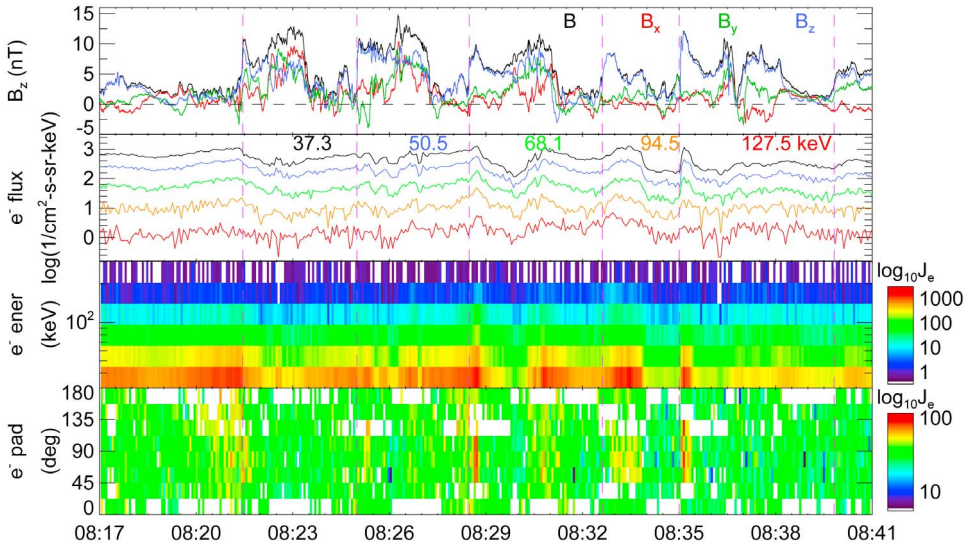

Figure 10. High-energy electron features observed during the event. From top to bottom: the magnetic field as a reference of the structure; electron differential fluxes at the center energies, 37.3, 50.5, 68.1, 94.5, and 127.5 keV; the energy spectrogram; and the pitch angle distribution. The vertical dashed lines demarcate the DFs.

quency (f_{lh}) to above the electron cyclotron frequency (f_{ce}). Figures 8c, 8f, and 8i show the electric field spectral power densities at times immediately ahead of or at DF 1, behind the DF, and (B_x, B_y) fluctuations, from top to bottom.

[26] Around the DF (Figures 8c and 8f) emissions near f_{lh} are evident. Lower hybrid drift waves are often generated by a diamagnetic current at a boundary that has a gradient in plasma density and temperature, which is characteristic of the DFs [*Zhou et al.*, 2009; *Sergeev et al.*, 2009]. Lower hybrid waves can heat electrons preferentially perpendicular to the magnetic field [*Ricci et al.*, 2004; *Daughton et al.*, 2004]. An additional peak at f_{ce} is noticeable behind the DF (Figure 8f). These electron cyclotron emissions could be linked to a ring-like (or shell-like) distribution indicated from Figure 8d [*Ashour-Abdalla and Kennel*, 1978], and appear to be coincident with the magnetic field maxima (for DF 3 and 4), possibly contributing to the generation of high-energy electrons (Figure 10) as discussed below. It is worth noting that the enhanced wave power below ~22 Hz is seen in the downstream region of the DF (see Figure 8i). These low-frequency electrostatic waves can effectively heat the ions behind the DF, primarily in the perpendicular direction to **B** B B by, for example, stochastic wave-particle interactions [*Ergun et al.*, 1999; *Lynch et al.*, 2002].

[27] Figure 10 shows high-energy (≳37 keV up to ~127.5 keV) electron fluxes. The particle fluxes increase ahead of DF 1 and immediately after DF 2, 3, and 5, and somewhat further behind the appearance of DF 4. Peaks in fluxes are often coincident with B_z maxima and these energetic electrons have pitch angles distributed mostly perpendicular/oblique (45°–135°) to the magnetic field, i.e., as shown in the bottom panel of Figure 10. An acceleration mechanism to produce several tens up to ≥100 keV electrons would need to be a secondary acceleration mechanism located at the magnetic pileup region, after an initial acceleration at the reconnection X line plus wave-particle interactions. The secondary process could be betatron acceleration [*Ashour-Abdalla et al.*, 2011], and/or nonadiabatic curvature and ∇**B** drifts [*Hoshino et al.*, 2001; *Hoshino*, 2005].

[28] Non-Maxwellian electron and ion distributions observed during the (B_x, B_y) fluctuations (Figures 8g–8i) may be unstable to a range of electrostatic and/or whistler instabilities. There appear to be whistler mode waves at frequencies of ~0.2 f_{ce} that are associated with ion beam-like components and/or field-aligned electron beams with strong temperature anisotropies [*Wong and Goldstein*, 1987, 1988; *Sazhin*, 1989; *Nishikawa et al.*, 1995]. Ion and electron energy increases at ~0826:30 UT in Figure 4f appear to be associated closely with wave activity (Figure 4e). A detailed analysis of the distributions and their association with the observed wave fluctuations will be studied further in future work.

3. Discussion

[29] We have reported Cluster observations of multiple injection boundaries of earthward fast flows and subsequent large (B_x, B_y) fluctuations that have peak amplitudes 1–2 min after each boundary crossing. Some earlier studies [e.g., *Ji and Wolf*, 2003a, 2003b; *Horton et al.*, 2004] explain that magnetic fluctuations such as Alfvénic fluctuations or Pi-2 turbulence associated with an earthward accelerated flux tube are driven by firehose instability due to a rapidly increasing temperature anisotropy, ($T_{\parallel} > T_{\perp}$) from the shortening of the magnetic field lines. That model, however, focuses on the magnetic fluctuations as the BBF brakes in the inner plasma sheet and cannot explain the characteristic behavior of the (B_x, B_y) fluctuations following DFs as observed in the present event.

[30] The fast earthward motion of BBFs or dipolarization/injection fronts have long been discussed in the context of the interchange instability [e.g., *Vasyliunas*, 1970]. Interchange instability associated with plasma transport in

Earth's plasma sheet involves magnetosphere-ionosphere (MI) coupling, as illustrated in Figure 9c. The interchange instability criteria has been studied by, e.g., *Bernstein et al.* [1958], *Gold* [1959], *Schmidt* [1979], *Volkov and Mal'tsev* [1986], and *Xing and Wolf* [2007], and it is often stated that interchange instability occurs when the gradients of flux tube entropy and flux tube volume are opposite. Consider the entire equatorial plane where both $\nabla(PV^{\gamma})$ and ∇V are generally pointing radially outward for an initially stable state (the *zeroth-order* gradients). The enhanced B_z flux tube behind a DF, often carrying a lower entropy content and having a smaller flux tube volume due to the jump in $|B|$, can be treated as a local disturbance to such zeroth-order $\nabla(PV^{\gamma})$ and ∇V in the *first order*. The first-order $\nabla(PV^{\gamma})$ and ∇V on the DF boundary can be directed oppositely to the zeroth-order ∇V and $\nabla(PV^{\gamma})$, respectively, which we conjecture may give rise to ripples. Initial small disturbances in the plasma boundary can generate small field-aligned currents that point oppositely on the two sides of the undulating ripple, $J_{\|} = -\hat{B} \cdot (\nabla P \times \nabla V) = -\hat{B} \cdot (\nabla(PV^{5/3}) \times \nabla V)/V^{5/3}$ [*Vasyliunas*, 1970]. These field-aligned currents are closed in the finite-conducting ionosphere, and the ionospheric electric field is coupled to the magnetosphere. Near the equatorial plane, the resulting $\mathbf{B}BE \times \mathbf{B}BB$ drift will then lead to growth of the initial disturbances.

[31] Figure 4k shows that the flux tube entropy decreases within enhanced B_z flux tubes behind a DF. We used three methods to estimate the entropy per magnetic flux tube volume (entropy parameter) and the local specific entropy. The entropy parameter, PV^{γ} shown in red in Figure 4k (where $\gamma = 5/3$, assuming temperature isotropy of an ideal monotonic gas) is derived from *Wolf et al.*'s [2006] formula for the estimation of the flux tube volume, V, using spacecraft measurements (One third of the estimated flux tube volume in a unit of R_E/nT is shown in green). The specific entropy parameter, $Pn^{-5/3}$ (where n is a local density measured by the spacecraft) is shown in blue. Classical thermodynamics relates the entropy parameter with thermodynamic entropy via the expression $S = -k_B \int F \ln F d^3\mathbf{v} d^3\mathbf{r}$ such that $PV^{5/3} \propto \exp(2S/3)$. The present event shows clearly that the entropy, S, calculated from the observed ion distribution functions (shown in black in Figure 4k) and the entropy parameter using *Wolf et al.*'s [2006] formula are both lower in the enhanced B_z flux tubes than in the ambient plasma. (Note that the thermal pressure downstream the DF might have been slightly underestimated due to a limited contribution from up to ~40 keV ions.) In contrast, the specific entropy parameter, $Pn^{-5/3}$, although having the form of flux tube entropy and using the local plasma density, does not differentiate the interior of the flux tube from the ambient plasma.

[32] On the DF boundaries, the gradient of the flux tube entropy is opposite to the zeroth-order ∇V. The flux tube volume estimated using *Wolf et al.*'s [2006] formula also decreases across DFs against the increasing background PV^{γ} along r. To quantitatively show that the DF is unstable to the interchange instability, we adopted *Bernstein et al.*'s [1958] criterion, $(\partial V - \mu_0 \partial P \int ds/B^3)(\partial V/V + \partial P/\gamma P) < 0$, which is valid for a 2-D axisymmetric, finite β plasma, therefore, is more appropriate for the plasma sheet than are other criteria. The second term in the first parenthesis is related to the variation of the plasma thermal pressure divided by magnetic pressure averaged over the flux tube. With an assumption that the measured β is an indicator of the average β, the interchange instability condition [*Bernstein et al.*, 1958] is found satisfied at all six DFs, but marginally for DF 4 and 6. (Note that the one-point measurement of near the equatorial plane can overestimate the flux tube averaged β. An improvement in this regard is worthwhile to pursue but left as future study.)

[33] The Bernstein criterion is, however, only valid when the two flux tubes are exactly parallel/antiparallel. This implies that the plasma sheet is interchange unstable almost everywhere, which is certainly not true. Thus it remains the satisfaction of the interchange instability criterion questionable and also makes it difficult to identify the interchange mode in the plasma sheet.

[34] Figure 11 shows wavelet scalograms for the corresponding magnetic disturbances during the event. Although the results are rather complicated, the following is noticeable. (1) Rather broadband enhancements at the times of DFs are present in B_z (mainly) and B_y. (2) The upstream DF signatures at a discrete frequency between 0.02 and 0.04 Hz that are continued by more intense and broad features in along with (B_x, B_y) fluctuations downstream of a DF are found in B_x. This is most clearly seen for DF 1, and is not identified in DFs 4 and 6 (the two DFs for which the Bernstein criterion is only marginally satisfied). The latter wavelet feature resembles previously reported in situ observations of a ballooning/interchange mode associated with magnetic dipolarization in the plasma sheet [*Saito et al.*, 2008b; *Park et al.*, 2010].

[35] Figure 12 shows the flow vectors projected onto the equatorial plane in the frame of each of the six DFs. Red, orange, yellow, green, sky blue, blue, and magenta arrows represent flow vectors at −12, −8, −4, 0, 4, 8, 12 s, respectively, relative to the time of a DF crossing. A vortical flow pattern is expected near the edge of the ripples in the magnetic disturbances if produced by interchange, but such a pattern is not obvious in the data. To detect such a pattern, however, requires that the spacecraft to be at the right locations with respect to the boundaries. Moreover, the spacecraft separation along the y direction is much smaller than the expected wavelength, ~3 R_E (estimated using the y directional propagation velocity of the structure and the transit time). Nevertheless, bearing in mind that interchange-associated deformation of the magnetic boundary will be accompanied by corresponding flow changes across the boundary, we note that upstream and downstream flow vectors are either directed oppositely or have large angles across the DFs except, again, DF 4 and 6.

[36] The consistent differences between DF 1–3 and 5 and DF 4 and 6, as demonstrated in the analyses of the Bernstein criterion, the wavelet scalograms, the flow patterns in the DF proper and the following large (B_x, B_y) fluctuations (which are absent following DF 4 and 6), indicate that the former DFs are probably unstable to interchange, while the latter ones are not. We also considered whether the large-amplitude (B_x, B_y) fluctuations detected after each DF passage could be a manifestation of tail flapping caused by the impact of the DF. We also considered whether the large-amplitude (B_x, B_y) fluctuations could be a manifestation of tail flapping caused by the impact of the DF, but the fluctuations do not show a typical tail-flapping signature, i.e., an

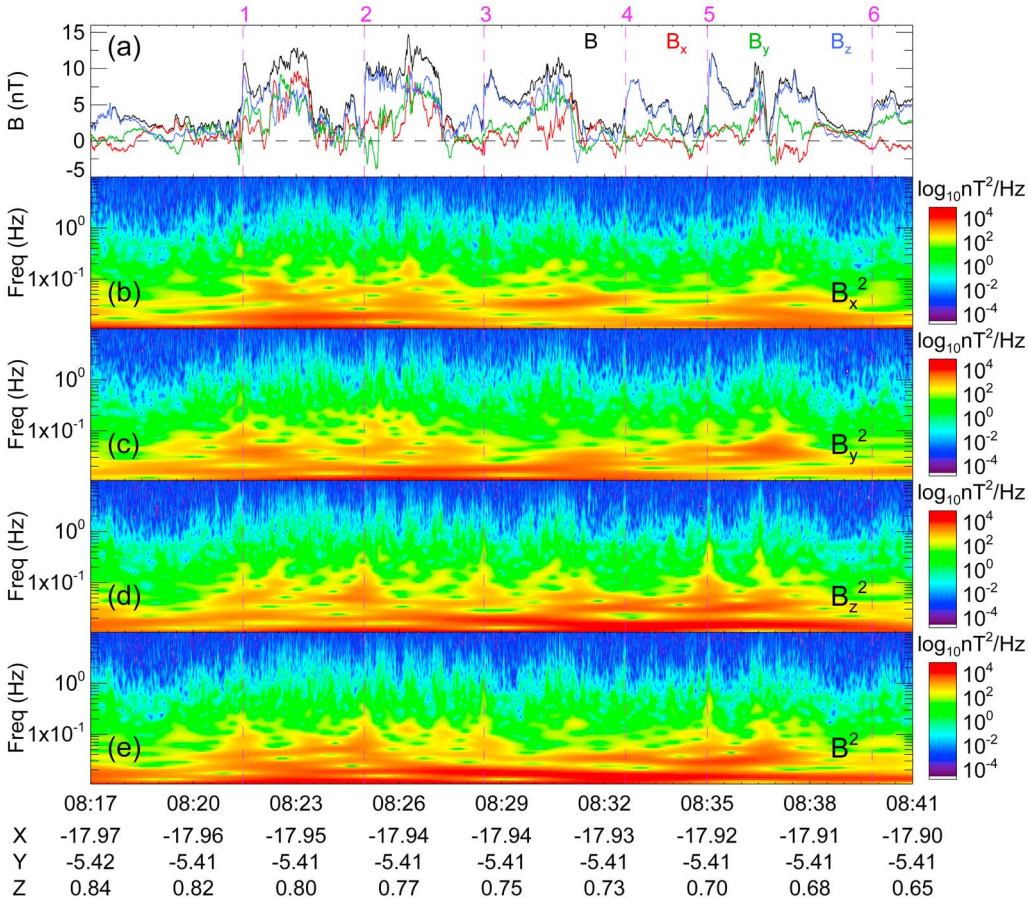

Figure 11. The wavelet scalograms for (b) B_x^2, (c) B_y^2, (d) B_z^2, and (e) B^2 for (a) the time series data of the magnetic field.

anticorrelation between $\delta B_x/\delta t$ and a bulk plasma velocity along the vertical direction to the current sheet ($\sim V_{z,\mathrm{GSM}}$) [*Sergeev et al.*, 2003].

[37] Therefore, we conclude that the fluctuations probably result from development of the interchange instability. Our observations show that the enhanced B_z flux tubes behind a DF carry a lower-content, lower-entropy plasma than the ambient plasma (Figure 9a). The leading edge of the enhanced B_z flux tube then becomes unstable to the interchange instability and starts to deform (Figures 9b and 9c), which generates field-aligned currents that possibly power auroral brightening after sequential MI-coupling processes (Figure 9c). In the context of this scenario, the observed 1–2 min interval between the DF passage and the (B_x, B_y) fluctuation peaks might correspond to the time scale for the interchange instability to develop.

[38] In Figure 3 we show IMAGE FUV images generated at an about 2 min cadence. The images show bead-like auroral brightening structures that start to develop within a few minutes of the Cluster observations of the first DF. While the large IMF-B_y component during the event and the tailward ($<-12\ R_E$) location of Cluster observations make it unreliable to estimate the foot point of the Cluster location using the T96 model [*Tsyganenko*, 1995], the correspondence in overall duration (~20 min) of the ionospheric features and Cluster observations might imply a link between the two regions with respect to MI coupling and ionospheric effects of the DFs occurring in the near-Earth magnetotail.

[39] It is worth noting that the ionospheric features appear to expand azimuthally, consistent with (B_x, B_y) fluctuation structures that might be expected as a result of the development of the deformation of the midtail plasma boundary via interchange. Figure 5 demonstrates that the (B_x, B_y) fluctuations (except the structure, "a") move duskward in the frame of the relevant DFs, as is expected since the propagation will have an increasing component along the dawn/dusk direction with time as the initial disturbance (ripple) becomes more corrugated (indicated in Figure 9b). One can also note that the background plasma upstream of each DF shows a dawnward flow at the velocities of ≥200 km/s. Therefore, the (B_x, B_y) fluctuations, including "a," propagate duskward in the frame of the background plasma. This explanation is consistent with numerical studies about the interchange/ballooning instability in the magnetotail [*Nakamura et al.*, 2002a; *Guzdar et al.*, 2010; *Pritchett and Coroniti*, 2010].

[40] The small-scale auroral emissions shown in Figure 3 were not followed by any substorm auroral breakup nor by any poleward expansion. Such signatures are often termed *pseudobreakup*. According to recent studies on multiple-

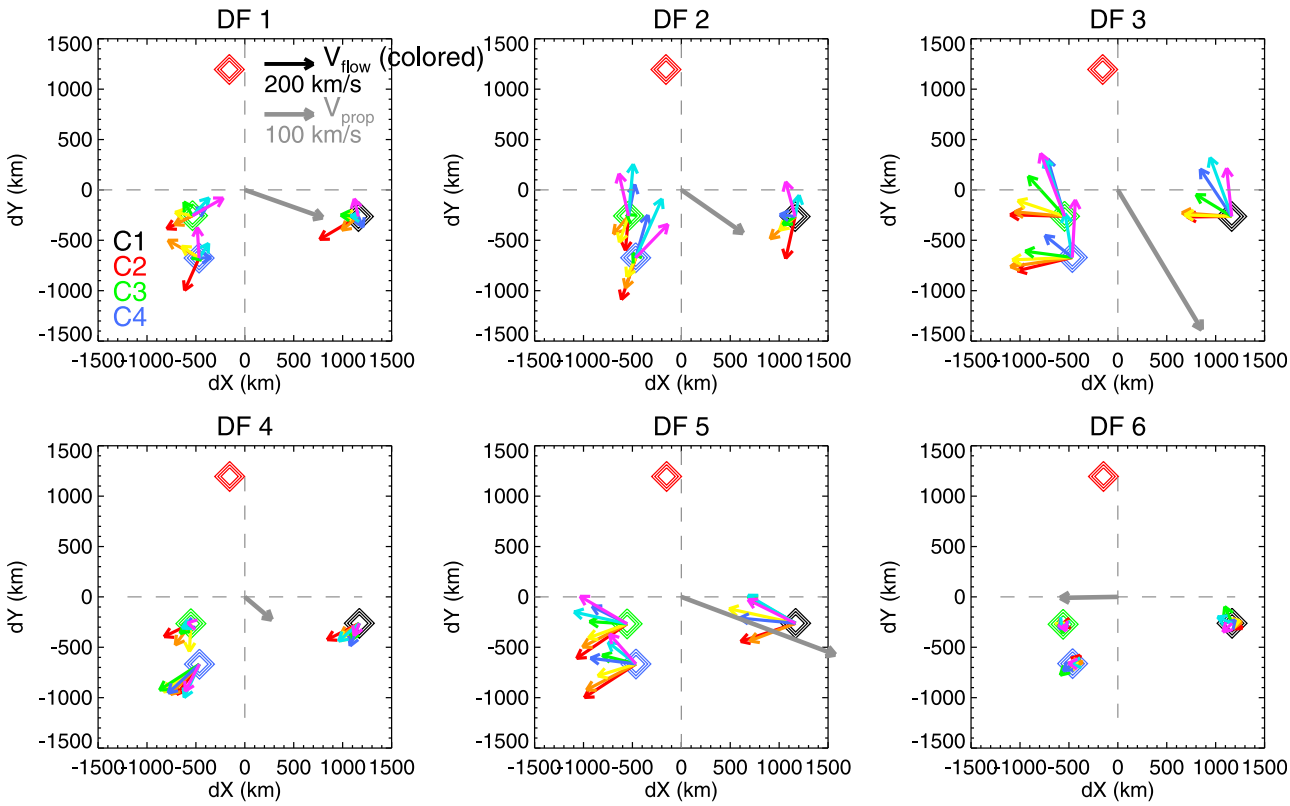

Figure 12. The relative flow vectors for the Cluster spacecraft (color-coded diamonds) with respect to each of the six DFs. Red, orange, yellow, green, sky blue, blue, and magenta arrows represent flow vectors measured at −12, −8, −4, 0, 4, 8, and 12 s, respectively, relative to the time of a DF crossing at each spacecraft's location (note that the instrument measuring ion moments is not available in C2).

onset substorms, the initial onset or pseudobreakup preconditions a major substorm onset by either generating a tailward propagating wave that triggers reconnection on the tailward side [*Saito et al.*, 2008a, 2010] or causing the plasma sheet to thin after transportation of existing plasmas into the inner magnetosphere [*Tang et al.*, 2010; *Nakamura et al.*, 2011]. These studies lead one to speculate that the initial DFs among the multiple DFs fail to precondition a major onset. The large multiplicity in 3–4 min might have lowered the efficiency of the impact of DFs on the substorm dynamics by being dissipated before reaching the inner plasma sheet boundary where a main onset might be triggered. Figure 4g shows that the density ratio of O^+ to H^+ increases from ~5% before the first DF to ~20% at the end of the event. This indicates that a series of bursty reconnection evolved from the plasma sheet to the lobe and that the repeated reconnection events on a short time scale might have leaked away free energy that could have been stored and released as a main substorm onset. Another possibility can be related to the patchiness of near-Earth tail reconnection. The observed multiple DFs can also result from patchy reconnection. Recent large-scale kinetic (LSK) simulations that use a global MHD code to calculate the electric and magnetic fields as a function of time, and then follow test particles [see, e.g., *Ashour-Abdalla et al.*, 1997, 2010], indeed show that the appearance of numerous reconnection sites dispersed over the near-Earth tail current sheet leads to a rapid decay of DF signatures in the inner plasma sheet region. Tout study of this event, therefore, provides insights into the effects of near-Earth tail reconnection and the relationship of DFs to substorms.

[41] The microphysical processes occurring at the DFs are described in this paper, but not completely. The exact nature of the instabilities and the wave generation mechanisms associated with the Hall-type microphysics together with their relationship to particle energization near the DF, the evolution of the BBF channel, and, ultimately, substorm dynamics are subjects for future study.

[42] **Acknowledgments.** This study was supported by NASA's MMS/IDS and Cluster missions at the Goddard Space Flight Center and by UMBC/GEST. We acknowledges all Cluster instrument teams, including PEACE, CIS, FGM, EFW, RAPID, WHISPER, and WIDEBAND staffs and the Cluster Active Archive (http://caa.estec.esa.int/caa). The authors acknowledge the referee correcting the estimation of the foot point of the Cluster location using the T96 model and both referee advising in using the interchange-instability criterion. K.-J. Hwang thanks Miho Saito for helpful discussions.

[43] Masaki Fujimoto thanks the reviewers for their assistance in evaluating this paper.

References

Angelopoulos, V., F. S. Mozer, T. Mukai, K. Tsuruda, S. Kokubun, and T. J. Hughes (1999), On the relationship between bursty flows, current disruption and substorms, *Geophys. Res. Lett.*, *26*, 2841.

Ashour-Abdalla, M., and C. F. Kennel (1978), Nonconvective and convective electron cyclotron harmonic instabilities, *J. Geophys. Res.*, *83*, 1531.

Ashour-Abdalla, M., et al. (1997), Ion sources and acceleration mechanisms inferred from local distribution functions, *Geophys. Res. Lett.*, *24*, 955.

Ashour-Abdalla, M., et al. (2010), Electron acceleration associated with inward moving dipolarization fronts, paper presented at Cluster 10th Anniversary-THEMIS Workshop, Eur. Space Agency, Corfu Island, Greece.

Ashour-Abdalla, M., M. El-Alaoui, M. L. Goldstein, M. Zhou, D. Schriver, R. Richard, R. Walker, M. G. Kivelson, and K.-J. Hwang (2011), Observations and simulations of non-local acceleration of electrons in magnetotail reconnection events, *Nat. Phys.*, doi:10.1038/nphys1903, in press.

Bernstein, I. B., E. A. Frieman, M. D. Kruskal, and R. M. Kulsrud (1958), An energy principle for hydromagnetic stability problems, *Proc. R. Soc. London, Ser. A*, *244*, 17.

Birn, J., and M. Hesse (1991), The substorm current wedge and field-aligned currents in MHD simulations of magnetotail reconnection, *J. Geophys. Res.*, *96*, 1611.

Daughton, W., G. Lapenta, and P. Ricci (2004), Nonlinear evolution of the lower-hybrid drift instability in a current sheet, *Phys. Rev. Lett.*, *93*, 105004, doi:10.1103/PhysRevLett.93.105004.

Ergun, R. E., C. W. Carlson, L. Muschietti, I. Roth, and J. P. McFadden (1999), Properties of fast solitary structures, *Nonlinear Processes Geophys.*, *6*, 187.

Gold, T. (1959), Motions in the magnetosphere of the Earth, *J. Geophys. Res.*, *64*, 1219.

Goldman, M. V., M. M. Oppenheim, and D. L. Newman (1999), Nonlinear two-stream instabilities as an explanation for auroral bipolar wave structures, *Geophys. Res. Lett.*, *26*, 1821.

Guzdar, P. N., A. B. Hassam, M. Swisdak, and M. I. Sitnov (2010), A simple MHD model of the formation of multiple dipolarization fronts, *Geophys. Res. Lett.*, *37*, L20102, doi:10.1029/2010GL045017.

Horton, W., B.-Y. Xu, and H. V. Wong (2004), Firehose driven magnetic fluctuations in the magnetosphere, *Geophys. Res. Lett.*, *31*, L06807, doi:10.1029/2003GL018309.

Hoshino, M. (2005), Electron surfing acceleration in magnetic reconnection, *J. Geophys. Res.*, *110*, A10215, doi:10.1029/2005JA011229.

Hoshino, M., T. Mukai, T. Terasawa, and I. Shinohara (2001), Superthermal electron acceleration in magnetic reconnection, *J. Geophys. Res.*, *106*, 25,972.

Ji, S., and R. A. Wolf (2003a), Firehose instability near substorm expansion-phase onset?, *Geophys. Res. Lett.*, *30*(24), 2242, doi:10.1029/2003GL017981.

Ji, S., and R. A. Wolf (2003b), Double-adiabatic MHD theory for motion of a thin magnetic filament and possible implications for bursty bulk flows, *J. Geophys. Res.*, *108*(A5), 1191, doi:10.1029/2002JA009655.

Keiling, A., et al. (2009), THEMIS ground-space observations during the development of auroral spirals, *Ann. Geophys.*, *27*, 4317.

Lui, A. T. Y. (1996), Current disruptions in the Earth's magnetosphere: Observations and models, *J. Geophys. Res.*, *101*, 13,067.

Lui, A. T. Y., R. E. Lopez, B. J. Anderson, K. Takahashi, L. J. Zanetti, R. W. McEntire, T. A. Potemra, D. M. Klumpar, E. M. Greene, and R. Strangeway (1992), Current disruptions in the near-Earth neutral sheet region, *J. Geophys. Res.*, *97*, 1461.

Lynch, K. A., J. W. Bonnell, C. W. Carlson, and W. J. Peria (2002), Return current region aurora: $E_{||}$, j_z, particle energization, and broadband ELF wave activity, *J. Geophys. Res.*, *107*(A7), 1115, doi:10.1029/2001JA900134.

Mende, S. B., et al. (2000), Far ultraviolet imaging from the IMAGE spacecraft, *Space Sci. Rev.*, *91*, 287.

Nakamura, M. S., H. Matsumoto, and M. Fujimoto (2002a), Interchange instability at the leading part of reconnection jets, *Geophys. Res. Lett.*, *29*(8), 1247, doi:10.1029/2001GL013780.

Nakamura, R., et al. (2002b), Motion of the dipolarization front during a flow burst event observed by Cluster, *Geophys. Res. Lett.*, *29*(20), 1942, doi:10.1029/2002GL015763.

Nakamura, R., A. Retinò, W. Baumjohann, M. Volwerk, N. Erkaev, B. Klecker, E. A. Lucek, I. Dandouras, M. André, and Y. Khotyaintsev (2009), Evolution of dipolarization in the near-Earth current sheet induced by earthward rapid flux transport, *Ann. Geophys.*, *27*, 1743.

Nakamura, R., et al. (2011), Flux transport, dipolarization and current sheet evolution during a double-onset substorm, *J. Geophys. Res.*, doi:10.1029/2010JA015865, in press.

Nishikawa, K.-I., O. Buneman, and T. Neubert (1995), New apsects of whistler waves driven by an electron beam studied by a 3-D electromagnetic code, *Adv. Space Res.*, *15*(12), 17.

Ohtani, S., K. Takahashi, L. J. Zanetti, T. A. Potemra, and R. W. McEntire (1992), Initial signatures of magnetic field and energetic particle fluxes at tail reconfiguration: Explosive growth phase, *J. Geophys. Res.*, *97*, 19,311.

Park, M. Y., D.-Y. Lee, S. Ohtani, and K. C. Kim (2010), Statistical characteristics and significance of low-frequency instability associated with magnetic dipolarizations in the near-Earth plasma sheet, *J. Geophys. Res.*, *115*, A11203, doi:10.1029/2010JA015566.

Paschmann, G., and P. W. Daly (1998), Analysis methods for multi-spacecraft data, *Sci. Rep. 001*, Int. Space Sci. Inst., Bern.

Pedersen, A., et al. (2008), Electron density estimations derived from spacecraft potential measurements on Cluster in tenuous plasma regions, *J. Geophys. Res.*, *113*, A07S33, doi:10.1029/2007JA012636.

Pickett, J. S., et al. (2005), On the generation of solitary waves observed by Cluster in the near-Earth magnetosheath, *Nonlinear Processes Geophys.*, *12*, 181.

Pritchett, P. L., and F. V. Coroniti (2010), A kinetic ballooning/interchange instability in the magnetotail, *J. Geophys. Res.*, *115*, A06301, doi:10.1029/2009JA014752.

Ricci, P., J. U. Brackbill, W. Daughton, and G. Lapenta (2004), Influence of the lower hybrid drift instability on the onset of magnetic reconnection, *Phys. Plasma*, *11*, 4489.

Runov, A., V. Angelopoulos, M. I. Sitnov, V. A. Sergeev, J. Bonnell, J. P. McFadden, D. Larson, K.-H. Glassmeier, and U. Auster (2009), THEMIS observations of an earthward-propagating dipolarization front, *Geophys. Res. Lett.*, *36*, L14106, doi:10.1029/2009GL038980.

Runov, A., et al. (2011), Dipolarization fronts in the magnetotail plasma sheet, *Planet. Space Sci.*, doi:10.1016/j.pss.2010.06.006, in press.

Sahraoui, F., M. L. Goldstein, P. Robert, and Y. V. Khotyaintsev (2009), Evidence of a cascade and dissipation of solar-wind turbulence at the electron gyroscale, *Phys. Rev. Lett.*, *102*, 231102, doi:10.1103/PhysRevLett.102.231102.

Saito, M. H., Y. Miyashita, M. Fujimoto, I. Shinohara, Y. Saito, and T. Mukai (2008a), Modes and characteristics of low-frequency MHD waves in the near-Earth magnetotail prior to dipolarization: Fitting method, *J. Geophys. Res.*, *113*, A06201, doi:10.1029/2007JA012778.

Saito, M. H., Y. Miyashita, M. Fujimoto, I. Shinohara, Y. Saito, K. Liou, and T. Mukai (2008b), Ballooning mode waves prior to substorm-associated dipolarizations: Geotail observations, *Geophys. Res. Lett.*, *35*, L07103, doi:10.1029/2008GL033269.

Saito, M. H., Y. Miyashita, M. Fujimoto, K. Liou, Y. Saito, and J. B. Sigwarth (2010), Stepwise feature of aurora during substorm expansion compared with the near-Earth tail dipolarization: Possible types of substorm dynamics, *J. Geophys. Res.*, *115*, A02207, doi:10.1029/2009JA014572.

Sazhin, S. S. (1989), Effects of ions and finite electron density on quasi-electrostatic whistler-mode propagation, *Astrophys. Space Sci.*, *158*, 107.

Schmidt, G. (1979), *Physics of High Temperature Plasmas*, 2nd ed., Academic, New York.

Sergeev, V., et al. (2003), Current sheet flapping motion and structure observed by Cluster, *Geophys. Res. Lett.*, *30*(6), 1327, doi:10.1029/2002GL016500.

Sergeev, V., V. Angelopoulos, S. Apatenkov, J. Bonnell, R. Ergun, R. Nakamura, J. McFadden, D. Larson, and A. Runov (2009), Kinetic structure of the sharp injection/dipolarization front in the flow-braking region, *Geophys. Res. Lett.*, *36*, L21105, doi:10.1029/2009GL040658.

Shiokawa, K., W. Baumjohann, and G. Haerendel (1997), Braking of high-speed flows in the near-Earth tail, *Geophys. Res. Lett.*, *24*, 1179.

Shiokawa, K., Y. Miyashita, I. Shinohara, and A. Matsuoka (2005), Decrease in B_z prior to the dipolarization in the near-Earth plasma sheet, *J. Geophys. Res.*, *110*, A09219, doi:10.1029/2005JA011144.

Sitnov, M. I., M. Swisdak, and A. V. Divin (2009), Dipolarization fronts as a signature of transient reconnection in the magnetotail, *J. Geophys. Res.*, *114*, A04202, doi:10.1029/2008JA013980.

Slavin, J. A., R. P. Lepping, J. Gjerloev, D. H. Fairfield, M. Hesse, C. J. Owen, M. B. Moldwin, T. Nagai, A. Ieda, and T. Mukai (2003), Geotail observations of magnetic flux ropes in the plasma sheet, *J. Geophys. Res.*, *108*(A1), 1015, doi:10.1029/2002JA009557.

Tang, C. L., V. Angelopoulos, A. Runov, C. T. Russell, H. Frey, K. H. Glassmeier, K. H. Fornacon, and Z. Y. Li (2010), Precursor activation and substorm expansion associated with observations of a dipolarization front by Thermal Emission Imaging System (THEMIS), *J. Geophys. Res.*, *115*, A07215, doi:10.1029/2009JA014879.

Tsyganenko, N. A. (1995), Modeling the Earth's magnetospheric magnetic field confined within a realistic magnetopause, *J. Geophys. Res.*, *100*, 5599.

Vasyliunas, V. M. (1970), Mathematical models of magnetospheric convection and its coupling to the ionosphere, in *Particles and Fields in the Magnetosphere*, edited by B. M. McCormac, p. 60, D. Reidel, Hingham, Mass.

Volkov, M. A., and Y. P. Mal'tsev (1986), A slot instability of the inner boundary of the plasma layer, *Geomagn. Aeron.*, *26*, 671.

Wolf, R. A., V. Kumar, F. R. Toffoletto, G. M. Erickson, A. M. Savoie, C. X. Chen, and C. L. Lemon (2006), Estimating local plasma sheet $PV^{5/3}$ from single-spacecraft observations, *J. Geophys. Res.*, *111*, A12218, doi:10.1029/2006JA012010.

Wong, H. K., and M. L. Goldstein (1987), Proton beam generation of whistler waves in the Earth's foreshock, *J. Geophys. Res.*, *92*, 12,419.

Wong, H. K., and M. L. Goldstein (1988), Proton beam generation of oblique whistler waves, *J. Geophys. Res.*, *93*, 4110.

Xing, X. (2008), Criterion for interchange instability in the plasma sheet, Ph.D. thesis, Rice Univ., Houston, Tex.

Xing, X., and R. A. Wolf (2007), Criterion for interchange instability in a plasma connected to a conducting ionosphere, *J. Geophys. Res.*, *112*, A12209, doi:10.1029/2007JA012535.

Zhou, M., M. Ashour-Abdalla, X. Deng, D. Schriver, M. El-Alaoui, and Y. Pang (2009), THEMIS observation of multiple dipolarization fronts and associated wave characteristics in the near-Earth magnetotail, *Geophys. Res. Lett.*, *36*, L20107, doi:10.1029/2009GL040663.

M. L. Goldstein and K.-J. Hwang, NASA Goddard Space Flight Center, Greenbelt, MD 20771, USA. (melvyn.l.goldstein@nasa.gov; kyoung-joo.hwang@nasa.gov)

E. Lee, Department of Astronomy and Space Science, Kyung Hee University, Yong-In, Kyung-Ki, 446-701, South Korea. (eslee@khu.ac.kr)

J. S. Pickett, Department of Physics and Astronomy, University of Iowa, Iowa City, IA 52242, USA. (pickett@uiowa.edu)